Dalton Transactions

PAPER

View Article Online
View Journal

Cite this: DOI: 10.1039/d5dt01251a

Constructing crystalline $NiCo_2O_4$/amorphous MoNiCo-LDH through high valence Mo doping for high-performance hybrid supercapacitors†

Juan Lei,[a] Yan Zhang,[b] Yujing Wang,[b] Xiaoli Ren,[a] Lijun Cheng,[a] Qinqin He[a] and Shuang Wang *[b]

Received 28th May 2025,
Accepted 7th July 2025

DOI: 10.1039/d5dt01251a

rsc.li/dalton

In this work, a crystalline/amorphous electrode material was prepared *via* a simple method. Specifically, high-valent Mo was introduced to fabricate amorphous MNC-LDH, which was then used to construct crystalline NCO/amorphous MNC-LDH composite materials. The prepared sample exhibited a three-dimensional pompom-like structure composed of ultrathin nanoflakes and a hybrid interface between crystalline and amorphous phases, which benefited its electrochemical performance. The synthesized material showed a specific capacity of 841 C g^{-1} at 1 A g^{-1}, while retaining 82.3% of its initial capacity at 20 A g^{-1}. The assembled NCO/MNC-LDH//AC HSC device exhibited an energy density of 58 Wh kg^{-1} when the power density was 850 W kg^{-1}. It is noteworthy that even at a power density of 8500 W kg^{-1}, an energy density of 37.1 Wh kg^{-1} was maintained. NCO/MNC-LDH//AC retained 76.3% of its initial specific capacitance and 100% coulombic efficiency after 20 000 consecutive charge and discharge cycles, demonstrating excellent cycling stability. Furthermore, the ability of two HSCs connected in series to power small fans and light LEDs in various colors indicated the material's practical application potential. The synthesized NCO/MNC-LDH thus demonstrates promise as a supercapacitor electrode material, providing valuable insights for designing crystalline/amorphous composites in electrochemical energy storage.

1. Introduction

It is widely recognized that enhancing the energy density of supercapacitors (SCs) requires the preparation of high-performance electrode materials. The electrochemical performance of electrode materials is influenced by many factors, for example, electrochemical redox activity, specific surface area, microscopic morphology and so on.[1] Phase engineering is a promising strategy for modifying physicochemical properties to further enhance the electrochemical properties of energy storage.[2,3] At present, much research on electrode materials mainly focuses on crystalline materials, but recent studies have shown that amorphous materials have significant characteristics in charge storage capacity that crystalline materials lack.

Due to the long-range disordered and short-range ordered arrangement of internal atoms, amorphous materials have more active sites and exhibit higher electrochemical activity.[4] At the same time, amorphous materials can provide more ion migration pathways without changing the lattice structure, promoting electrochemical reactions.[5,6] Crystalline materials have higher electrical conductivity and stability than amorphous materials.[7–11] However, the infiltration and diffusion of ions are restricted by the compact arrangement of surface atoms, which limits their electrochemical activity.[12] The interactions formed between the different components of the crystalline and amorphous phases give them special properties. Therefore, constructing crystalline/amorphous materials is a promising strategy, which can combine the advantages of both materials to achieve a balance of electrochemical activity and stability.[13] For example, the crystalline $NiCo_2O_4$@amorphous$NiCo_2S_4$ heterostructure constructed by Wang *et al.* showed a specific capacity of 1121.5 C g^{-1} at 1 A g^{-1}, which was much higher than that of $NiCo_2O_4$ (197.0 C g^{-1}) and $NiCo_2S_4$ (193.65 C g^{-1}).[14] Huang *et al.* prepared amorphous/crystalline NiCoB@$NiCo_2S_4$ that exhibited a specific capacity of 781 C g^{-1} at 1 A g^{-1}, which was higher than that of NiCoB and NiCoB-LDH alone. In addition, after 10 000 charge and discharge times, the capacity retention rate of NiCoB@$NiCo_2S_4$ was 78%, while the capacity retention rate of NiCoB-LDH was only 51% after 3000 charge and discharge cycles, and the capacity retention rate of NiCoB was 64.8% after 7000 charge and discharge cycles.[15]

Therefore, it is necessary to develop a simple and easy method for constructing crystalline/amorphous composites. In

---

[a] *Department of Environmental and Safety Engineering, Taiyuan Institute of Technology, Taiyuan 030018, Shanxi Province, P.R. China*
[b] *College of Environment and Ecology, Taiyuan University of Technology, Jinzhong 030600, Shanxi Province, P.R. China. E-mail: wangshuang@tyut.edu.cn*

† Electronic supplementary information (ESI) available. See DOI: **https://doi.org/10.1039/d5dt01251a**

addition, heteroatom doping can change the crystal structure of the material itself and is an effective way to prepare amorphous materials.[16] It is a good choice to introduce high-valence metal doping based on previous studies.[17–19] Among them, Mo is a good choice. On the one hand, it is a non-three-dimensional high-valence metal and has special advantages in optimizing electrochemical properties and Gibbs free energy (ΔG) generated by electrocatalytic intermediates.[20–22] On the other hand, the similar atomic structure of Mo, Ni and Co atoms is very favorable for doping reactions.[23] At present, crystalline/amorphous materials have been synthesized for SCs, but there is still room for improvement in energy density, which may be due to the unsatisfactory structural design, and the construction of three-dimensional structures is conducive to the improvement of performance.

Based on these ideas, a crystalline NCO/amorphous MNC-LDH composite was constructed by a hydrothermal method, in which amorphous MNC-LDH was achieved by introducing Mo. Its unique structure has the following advantages: (i) the three-dimensional pompom-like structure composed of ultrathin nanoflakes can provide a large specific surface area, expose more active area, facilitate electrolyte penetration and shorten the ion diffusion distance; (ii) abundant active sites at the interface composed of crystalline and amorphous phase structures are conducive to the improvement of performance; (iii) the synergistic effect resulting from the composite formation of metal oxides and metal hydroxides contributes to enhanced electrochemical performance. As a result, the prepared crystalline NCO/amorphous MNC-LDH composite shows an improved electrochemical performance. Furthermore, the hybrid supercapacitor (HSC) device made of the prepared composite materials and activated carbon (AC) exhibited a high energy density of 58 Wh kg^{-1} at a power density of 850 W kg^{-1} and a capacitance retention rate of 76.3% after 20 000 charging and discharging cycles. Therefore, the prepared composite in this work exhibited good electrochemical properties and great potential for application in SCs, which provides an effective way for the construction of crystalline/amorphous composite materials.

2. Experimental procedures

2.1. Materials and reagents

$Ni(NO_3)_2·6H_2O$ (99%) was purchased from Sinopharm Chemical Reagent Co., Ltd, $Co(NO_3)_2·6H_2O$ (99%), $Na_2MoO_4·2H_2O$ (99%), NH_4F (98%), $CO(NH_2)_2$ (≥99.5%) and activated carbon (AC) were purchased from Shanghai Aladdin Biochemical Technology Co., Ltd. Polytetrafluoroethylene (60%), acetylene black (battery level) and diaphragm were purchased from the Lizhiyuan Branch of Yingze District, Taiyuan City, China. The nickel foam (NF, 99.8%) was purchased from Tianjin EVS Chemical Technology Co., Ltd. The NF was pretreated with 3 M hydrochloric acid, acetone and ethanol by ultrasonic treatment for 10 min, and then ultrasonic treatment with deionized (DI) water until pH = 7, and finally dried in a vacuum drying oven at 60 °C for 6 h.

2.2. Synthesis of $NiCo_2O_4$ nanoneedles

The $NiCo_2O_4$ nanoneedles were obtained by a hydrothermal method. First, in 15 mL of deionized (DI) water, 0.3 mmol of $Ni(NO_3)_2·6H_2O$, 0.6 mmol of $Co(NO_3)_2·6H_2O$, 2.4 mmol of $CO(NH_2)_2$ and 0.4 mmol of NH_4F were added to obtain a homogeneous solution after stirring for 2 h. After that, pre-treated NF (2 × 2.2 cm^2) was placed in an autoclave with the homogeneous solution and allowed to react for 5 h at 120 °C. After the reaction was completed, the $NiCo_2O_4$ precursor was uniformly grown on the NF after washing and drying. Finally, the final product was achieved by calcining in a muffle furnace for 2 h at 350 °C. Since mass loading affects electrochemical performance, we computed the mass difference of NF before and after the reaction to determine the mass loading of the active ingredient. The mass loading of $NiCo_2O_4$ grown on NF was 1.1 mg cm^{-2}. For convenience, the sample was labeled NCO.

2.3. Synthesis of the $NiCo_2O_4$/MoNiCo-LDH composite

The $NiCo_2O_4$/MoNiCo-LDH composite was synthesized by a secondary hydrothermal method. Specifically, 0.045 mmol of $Na_2MoO_4·2H_2O$, 0.135 mmol of $Ni(NO_3)_2·6H_2O$, 0.27 mmol of $Co(NO_3)_2·6H_2O$, 2.25 mmol of $CO(NH_2)_2$ and 0.83 mmol of NH_4F were dissolved in 15 mL of DI water. Stirring was necessary for obtaining a transparent solution. Then the homogeneous solution and a piece of NF with NCO were placed in an autoclave and reacted at 100 °C for 4 h. Then, the product was sonicated with ethanol and DI water and dried for 6 h at 60 °C. For comparison, NiCo-LDH, MoNiCo-LDH and $NiCo_2O_4$/NiCo-LDH were also synthesized by the above method (details are given in the ESI†). The mass loadings of $NiCo_2O_4$/MoNiCo-LDH, NiCo-LDH, MoNiCo-LDH and $NiCo_2O_4$/NiCo-LDH were 2.1, 1.3, 1.0 and 1.6 mg cm^{-2}, respectively. The samples were named NCO/MNC-LDH, NC-LDH, MNC-LDH and NCO/NC-LDH, respectively.

2.4. Characterization of materials

The crystal structure was investigated by powder X-ray diffraction (XRD, PANalytical Aeris X). X-ray photoelectron spectroscopy analysis was conducted to determine the valence state and composition of chemicals (XPS, Thermo Scientific K-Alpha). The specific surface area and pore size distribution were obtained through BET testing (BET, Micromeritics TriStar II 3020). The morphology was examined using a scanning electron microscope (SEM, JSM-7900F) and a transmission electron microscope (JEOL JEM-F200).

2.5. Electrochemical measurements

A VersaSTAT3 electrochemical workstation was used to study the electrochemical performance of samples in three- and two-electrode systems. The working electrode, reference electrode, and counter electrode were the prepared samples, platinum mesh, and Hg/HgO electrode, respectively. 6 mol L^{-1} KOH was used as an electrolyte. Cyclic voltammetry (CV) was performed at different scan rates (10–50 mV s^{-1}) in a fixed voltage window (0–0.6 V). Charge–discharge tests (GCD) were carried out under a voltage window of 0–0.5 V, with a current density of 1–20 A g^{-1}. Electrochemical impedance spectroscopy (EIS) was carried out in the frequency range of 0.01–10^5 Hz with an amplitude of 5 mV on a LANHE CT3001A.

The following formula was utilized to determine the specific capacity (C g^{-1}):[24]

$$Q = \frac{I \times \Delta t}{m} \tag{1}$$

Additionally, the following formula was used to calculate the specific capacitance (F g^{-1}) of HSC devices:

$$C = \frac{I \times \Delta t}{m \times \Delta V} \tag{2}$$

where I (A) represents the discharge current, Δt (s) represents the discharge time, m (g) represents the mass loading of the active material, and ΔV (V) is the voltage window.

2.6. Fabrication of the all-solid-state HSC device

An all-solid-state HSC device was constructed with NCO/MNC-LDH and AC as positive and negative electrodes and PVA/KOH gel as the electrolyte. The negative electrode was prepared in the following manner: 80 mg of AC, 10 mg of acetylene black, and 7 μL of PTFE lotion were added into an agate mortar. After mixing in a specified quantity of ethanol, the mixture was ground for approximately 1 h to create a homogeneous slurry. After making the paste, it was spread equally on NF (2 × 2.2 cm^2), dried for 6 h at 60 °C in an oven, and then pressed at 10 MPa. Next, the gel electrolyte was made using the subsequent procedure: after dissolving 1.5 g of KOH in 30 mL of deionized water and heating the mixture to 85 °C to create a transparent solution, 3.0 g of PVA was added, and the mixture was heated further to create a homogeneous and translucent gel. A layer of gel was coated onto the surface of the positive electrode, followed by placing a separator to prevent short circuits. Another layer of gel was then applied and finally covered with the negative electrode. The mass matching of positive and negative electrodes should satisfy the charge balance condition $q^+ = q^-$ (q^+: charge of the positive electrode; q^-: charge of the negative electrode).[25] The mass matching formula may be used to determine the mass loading of the positive and negative electrodes:[26]

$$\frac{m^+}{m^-} = \frac{C^- \times \Delta V^-}{Q^+} \tag{3}$$

where m^+ (g) and Q^+ (C g^{-1}) represent the mass loading and specific capacity of the positive electrode, while m^- (g), C^- (F g^{-1}) and ΔV^- (V) are the mass loading, specific capacitance, and operating potential window of the negative electrode, respectively.

The following formulas are used to determine the specific capacitance (C, F g^{-1}), energy density (E, Wh kg^{-1}), and power density (P, W kg^{-1}) of HSC devices:[27,28]

$$C = \frac{I \times \Delta t}{m \times \Delta V} \tag{4}$$

$$E = \frac{C \times \Delta V^2}{2 \times 3.6} \tag{5}$$

$$P = \frac{E}{\Delta t} \times 3600 \tag{6}$$

where I (A), Δt (s), m (g) and ΔV (V) represent the discharge current, the discharge time, the mass loading of the HSC device and the operating potential window, respectively.

3. Results and discussion

3.1. Characterization of the structure and morphology

Fig. 1 illustrates the preparation process of NCO/MNC-LDH. Urea was hydrolyzed at a high temperature to produce OH^- and CO_3^{2-}, which created an alkaline environment for the reaction. The addition of ammonium fluoride promoted the growth of crystal particles on the NF. Under these conditions, the NCO precursor grew on the NF.[29] Secondly, after the subsequent drying and calcination processes, uniform NCO nanowire arrays were grown on the NF. Finally, the three-dimensional pompom-like NCO/MNC-LDH composite material was synthesized through secondary hydrothermal and drying processes.

SEM was used for monitoring the morphological evolution of samples. The NCO nanowire arrays were uniformly distributed on the NF framework (Fig. 2a and b), while NC-LDH exhibited a flower-like shape composed of interwoven nanosheets (Fig. 2c and d).

The morphology of NC-LDH obviously changed after the introduction of Mo sources. Numerous nanosheets assembled into hydrangea-like nanoflowers, and the nanosheets became thinner and smaller (Fig. 2e and f). The NCO/NC-LDH composite material was synthesized *via* a secondary hydrothermal process. It could be observed that NC-LDH nanosheets grew on the surface of the NCO nanoneedle arrays. Despite the larger size and smoother surface of the nanosheets, the material retained its three-dimensional structure (Fig. 2g and h). When NCO was combined with MNC-LDH, the latter covered the surface of NCO to form the NCO/MNC-LDH composite material with a pompom-like shape. The ultrathin nano-

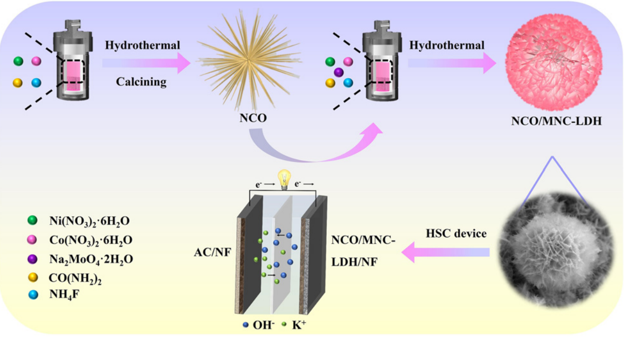

Fig. 1 Schematic illustration of the synthesis of NCO/MNC-LDH.

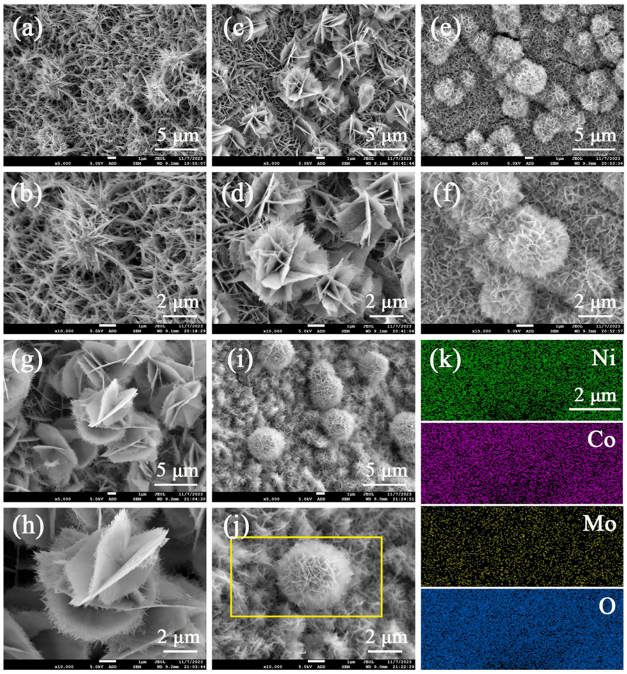

Fig. 2 SEM images of (a and b) NCO; (c and d) NC-LDH; (e and f) MNC-LDH; (g and h) NCO/NC-LDH; (i and j) NCO/MNC-LDH; and (k) EDS elemental mapping images of Ni, Co, Mo, and O in NCO/MNC-LDH.

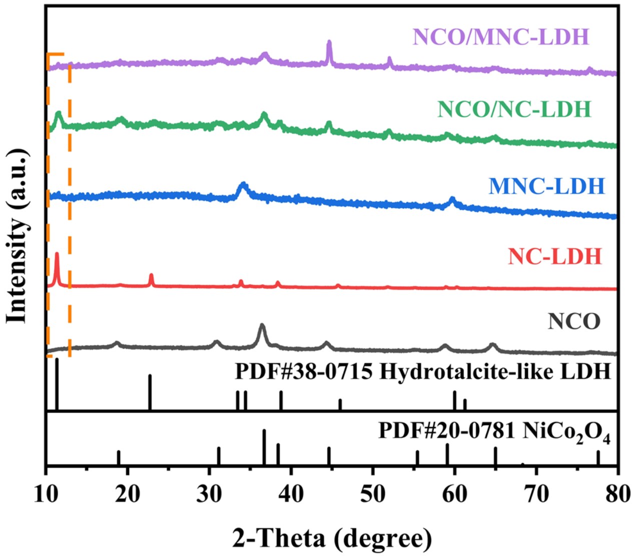

Fig. 3 XRD patterns of NCO/MNC-LDH, NCO/NC-LDH, MNC-LDH, NC-LDH and NCO.

flakes that make up the three-dimensional pompom-like structure could improve the specific surface area, thereby facilitating the redox reaction and accelerating the penetration of electrolyte into the electrode material. Furthermore, the consistent distribution of Ni, Co, Mo, and O in NCO/MNC-LDH was demonstrated by the area-selected EDS elemental maps displayed in Fig. 2k.

XRD was used for analyzing crystal phase compositions. As shown in Fig. 3, the diffraction peaks of NCO and NC-LDH could correspond to their standard cards of PDF#20-0781 and PDF#38-0715,[30,31] respectively, and the diffraction peaks were sharp, indicating their crystalline characteristics. The peaks of NC-LDH at 11.3° and 22.7° corresponded to the (003) and (006) crystal planes, which were indicative of the layered structure of LDH.[32] These two peaks disappeared after the introduction of Mo, leaving only two broad peaks near 33.5° and 59.9°, corresponding to the (101) and (110) crystal planes, respectively. This phenomenon likely indicated a reduction in the crystallinity of NC-LDH and its transformation into an amorphous material, while partially retaining the layered structure in the form of randomly dispersed nanosheets.[33] This observation was further corroborated by the subsequent TEM results. The diffraction peaks of NCO/MNC-LDH indicated that crystalline NCO and the amorphous MNC-LDH composite were successfully prepared. In addition, two small peaks located at 51.8° and 76.4° were also observed, which may be attributed to Ni. Fig. S2† displays the FTIR spectrum of NCO/MNC-LDH. The vibrational absorption peak at 3445 cm^{-1} was attributed to the stretching vibrations of O–H bonds within the material.[34] The peak observed at 1600 cm^{-1} was associated with water molecules adsorbed on the material surface.[35] The presence of interlayer carbonate anions (CO_3^{2-}) resulted in stretching and bending peaks at 1634 cm^{-1} and 776 cm^{-1}, respectively. Peaks located at 647 cm^{-1} and 553 cm^{-1} were assigned to the vibrations of the Ni–O and Co–O bonds, respectively.[36] The minor peaks at 1117 cm^{-1} and 1155 cm^{-1} were attributed to C–N bond stretching vibrations, while the peaks at 2831 cm^{-1} and 2717 cm^{-1} were assigned to C–H bond stretching.[37]

The microstructure of NCO/MNC-LDH was observed through TEM and HRTEM. Fig. 4a clearly reveals that the composite was composed of wrinkled and stacked nanosheets. The HRTEM images of region 1 and region 2 are shown in Fig. 4b and c, respectively.

Apparently, the crystalline–amorphous interfaces between NCO and MNC-LDH were observed, where one side was a crystalline region, and the other was an amorphous region. In the crystalline region, the calculated interlamellar distance of 0.29 nm corresponded to the (220) crystal plane of NCO, while no obvious lattice fringes were observed in the amorphous region. In addition, the transition zone from the crystalline region to the amorphous region was also proved by the corresponding inverse fast Fourier transformation (IFFT) and fast Fourier transform (FFT) patterns.

It was evident that the clear lattice fringes of IFFT shown in Fig. 4b1 and c3 represented the crystalline zone (NCO), and the fuzzy patterns of IFFT shown in Fig. 4b3 and c1 represented the amorphous zone (MNC-LDH), respectively. Moreover, Fig. 4b2 and c2 containing both clear lattice fringes and fuzzy patterns indicate the interfaces between crystalline and amorphous phases. Similarly, the FFT images shown in Fig. 4b1–3 and c1–3 also easily distinguished the crystalline

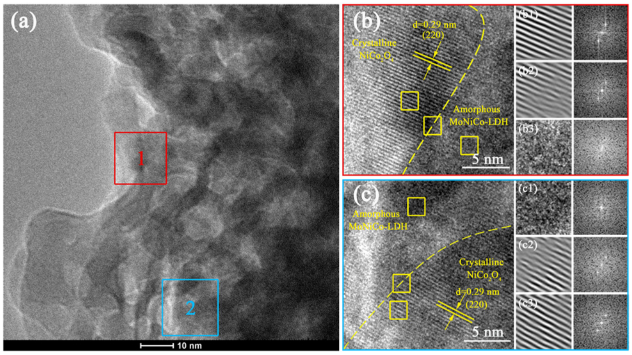

Fig. 4 TEM images of (a) NCO/MNC-LDH; HRTEM images of (b) region 1 and (c) region 2; IFFT and FFT of region 1 (b1–b3) and region 2 (c1–c3).

phases. These observations indicated that there were many interfaces between the crystalline and amorphous phases in the composite, which correlated well with the XRD results, once again confirming the synthesis of crystalline/amorphous composite materials.

The valence states and chemical composition were examined through XPS. Fig. S3† exhibits the XPS full spectrum of NCO/MNC-LDH, with characteristic peaks of Ni, Co, Mo, and O elements present, confirming the elemental composition of the sample. Ni 2p spectra in Fig. 5a could be fitted as two satellite peaks and two spin doublet peaks. Ni^{2+} was represented by the combined energies of 855.36 and 873.05 eV, and Ni^{3+} was represented by the combined energies of 856.68 and 874.61 eV.[38] Similarly, two spin doublet peaks and two satellite peaks could also be used to match the Co 2p spectrum. Peaks with binding energies of 782.55 and 797.79 eV were associated with Co^{2+} species, whereas peaks at binding energies of 780.65 and 796.24 eV were associated with Co^{3+} species (Fig. 5b).[39] The peaks with binding energies of 232.05 and 235.2 eV in the Mo 3d spectrum were related to Mo^{6+}, indicating the introduction of Mo^{6+} into the sample (Fig. 5c).[40] Three peaks could be distinguished in the O 1s spectrum, with O_M at the binding energy of 529.9 eV representing metal–oxygen bonds, $O_{OH/V}$ at 531.0 eV representing oxygen vacancies sites and hydroxyl oxygen species, and O_W at 532.0 eV representing adsorbed water molecules (Fig. 5d).[41] The presence of $O_{OH/V}$ indicated the possibility of oxygen defects, which were related to the crystal phase changes caused by the doping of metal ions.

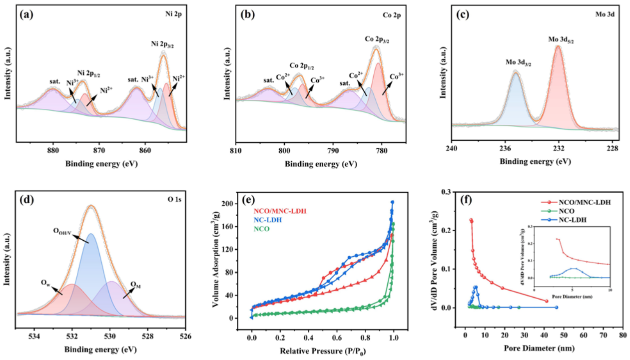

Fig. 5 The high-resolution XPS spectra of (a) Ni 2p; (b) Co 2p; (c) Mo 3d; (d) O 1s; (e) N_2 adsorption–desorption isotherms; and (f) the Barrett–Joyner–Halenda (BJH) pore size distribution plots of NCO/MNC-LDH, NC-LDH and NCO.

Furthermore, NCO/MNC-LDH, NC-LDH, and NCO samples were subjected to BET testing to examine their pore structure and specific surface area. The mesoporous characteristics of the three samples are evident in Fig. 5e, in which they displayed type IV adsorption–desorption isotherms and clear H3 hysteresis loops within the P/P_0 range of 0.45–1.0 relative pressure.[42] The isotherm of NCO/MNC-LDH showed a bigger hysteresis loop, which suggested that there were more mesopores.[43] NCO/MNC-LDH, NC-LDH, and NCO exhibited specific surface areas (SSAs) of 101.1, 118.3, and 27.8 $m^2 g^{-1}$, respectively. NCO/MNC-LDH showed a big specific surface area and further proved their mesoporous properties (Fig. 5f). In addition, NCO/MNC-LDH had the largest pore volume. Consequently, Mo doping had a significant impact on pore volume and SSA, which was vital for enhancing electrochemical performance. The specific capacity, energy density, and power density may all be increased by the bigger SSA by accelerating the kinetics of electron and ion transport. Furthermore, high porosity could accelerate the penetration of the electrolyte and thus improve the wettability of the material. In the case of electrolyte infiltration, active substances fully participated in the reaction, leading to the formation of an extended electrode–electrolyte interface, which was beneficial for Faraday redox reactions, especially at higher scan rates.[44]

3.2. Electrochemical properties

Electrochemical performance was examined in a three-electrode system with 6 mol L^{-1} KOH. The conductivity of 6 mol L^{-1} KOH electrolyte at room temperature was 177.1 mS cm^{-1}. First, the electrochemical performance of bare NF was evaluated, and it was charged and discharged in a relatively short period of time, so the effect of its specific capacity on the electrode material was negligible (Fig. S4†). The CV curves of NCO/MNC-LDH at 10–50 mV s^{-1} are displayed in Fig. 6a. The presence of two prominent redox peaks and a distinct voltage difference on the CV curve indicated the battery-type characteristics of the electrode material.[45] The ohmic polarization phenomenon caused the oxidation and reduction peaks to slightly shift as the scan rate increased.[46] However, the CV curves retained their stable shape even at high scan rates, indicating good reversibility of the redox reaction. The GCD curve of NCO/MNC-LDH at various current densities (1–20 A g^{-1}) is displayed in Fig. 6b. The clear charge–discharge platform was associated with the charge-transfer mechanism and the electrochemical reaction at the electrode–electrolyte interface, indicating its battery-type properties consistent with the CV results. The energy storage process of NCO/MNC-LDH was driven by the Faraday reduction reaction involving Ni^{2+}/Ni^{3+},

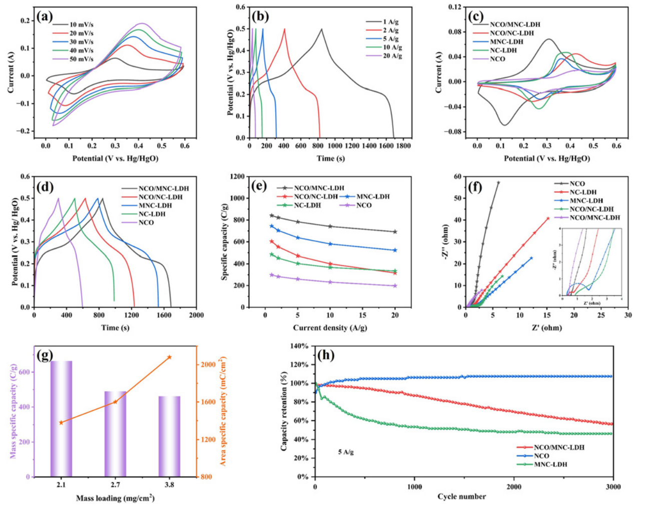

Fig. 6 (a) CV curves of NCO/MNC-LDH at 10–50 mV s^{-1}; (b) GCD curves of NCO/MNC-LDH at 1–20 A g^{-1}; (c) CV curves of NCO/MNC-LDH, NCO/NC-LDH, MNC-LDH, NC-LDH and NCO at 10 mV s^{-1}; (d) GCD curves of NCO/MNC-LDH, NCO/NC-LDH, MNC-LDH, NC-LDH and NCO at 1 A g^{-1}; (e) specific capacities at different current densities of NCO/MNC-LDH, NCO/NC-LDH, MNC-LDH, NC-LDH and NCO; (f) Nyquist plots of NCO/MNC-LDH, NCO/NC-LDH, MNC-LDH, NC-LDH and NCO; (g) mass specific capacity and area specific capacity at different mass loadings of NCO/MNC-LDH; and (h) cycling performance of NCO/MNC-LDH, MNC-LDH and NCO.

Co^{2+}/Co^{3+}, and Co^{3+}/Co^{4+}, which was explained by the following chemical reaction equations:[47,48]

$$NiCo_2O_4 + OH^- + H_2O \leftrightarrow NiOOH + 2CoOOH + e^- \tag{7}$$

$$Ni(OH)_2 + OH^- \leftrightarrow NiOOH + H_2O + e^- \tag{8}$$

$$Co(OH)_2 + OH^- \leftrightarrow CoOOH + H_2O + e^- \tag{9}$$

$$CoOOH + OH^- \leftrightarrow CoO_2 + H_2O + e^- \tag{10}$$

The CV curves of NCO/MNC-LDH, NCO/NC-LDH, MNC-LDH, NC-LDH, and NCO at 10 mV s^{-1} are displayed in Fig. 6c. The bigger region surrounded by the NCO/MNC-LDH CV curve suggested that it showed a higher specific capacity. Fig. 6d shows the GCD curves at a current density of 1 A g^{-1}. NCO/MNC-LDH showed the longest discharge time, with an estimated specific capacity of 841 C g^{-1} (1682 F g^{-1}), which was larger than that of the other materials. The CV and GCD curves for NCO, NC-LDH, MNC-LDH and NCO/NC-LDH are displayed in Fig. S5.† The main reasons for its improved capacity were the increased specific surface area of NCO/MNC-LDH, the expanded ion transport channels of the amorphous materials, and the exposure of more active redox reaction sites by the crystalline/amorphous composite interface. In addition, the capacity retention of different samples at 1–20 A g^{-1} was studied (Fig. 6e). NCO/MNC-LDH maintained 82.3% specific capacity at 20 A g^{-1}, which was higher than that of NCO/NC-LDH (52.4%), MNC-LDH (70%), NC-LDH (68.9%) and NCO (66.4%), respectively (Table S2†).

Fig. 6f shows the Nyquist plots of samples and the corresponding impedance fitting circuit model is displayed in Fig. S6.† The internal resistance (R_s) was represented by the intercept of the semicircle at the junction of the X-axis, the charge transfer resistance (R_{ct}) was represented by the semicircle, and the Warburg resistance (R_w) was represented by the slope of the line in the low frequency zone.[49] The resistance values of each component of the material may be determined by fitting the equivalent circuit model, and the results are displayed in Table S3.† Compared with the other four materials, NCO/MNC-LDH exhibited a lower R_{ct} value of 0.01 Ω, indicating faster electrochemical reaction kinetics. The correlation between the R_{ct} and the quantity of active sites on the surface of the materials indicated that the interface created by the prepared crystalline/amorphous composite material contained a large number of active sites. Additionally, in the low-frequency region, NCO/MNC-LDH exhibited a larger straight slope, indicating that it showed a smaller diffusion resistance and therefore a faster ion diffusion rate. This may be due to the high specific surface area and porous structure, which favored reactant adsorption and expedited ion transport. Moreover, the mass specific capacity and area specific capacity were also examined under various mass loading conditions. The mass specific capacity was inversely related to mass loading and decreased as the mass loading increased, whereas the mass loading was positively correlated with the area specific capacity (Fig. 6g and Fig. S7†). When the mass loading was 2.1, 2.7 and 3.8 mg cm^{-2}, the corresponding mass specific capacities were 665, 490.5 and 461.5 C g^{-1}, respectively, and the corresponding area specific capacities were 1380, 1600 and 2080 mC cm^{-2} at 5 A g^{-1}, respectively. With the increase of mass loading, the electrode material still maintained a high specific capacity, proving its good energy storage capacity. The stability of NCO/MNC-LDH, NCO, and MNC-LDH after continuous charge and discharge cycles is shown in Fig. 6h. After undergoing 3000 consecutive charge–discharge cycles at 5 A g^{-1}, the NCO/MNC-LDH composite exhibited a capacity retention rate between those of NCO and MNC-LDH, demonstrating acceptable cycling stability of the composite material. In addition, the conductive resistance of the sample after the cycle increased because of the structural change during the cycles (Fig. S8†).

3.3. Reaction kinetics analysis

The Dunn equation is used to analyze the relationship between the anode and cathode peak current density (i) and scan rate (ν).[50]

$$i = a\nu^b \tag{11}$$

Here, the values of a and b are determined by linear fitting of peak current density and the logarithm of the scan rate of CV curves. Generally speaking, charge storage is mostly diffusion controlled when b = 0.5 and surface capacitance controlled when b = 1. The b value of anodic slopes of NCO/MNC-LDH is 0.72, which indicates that it is impacted by both surface capacitance-controlled processes and diffusion-controlled processes (Fig. 7a).

We also tested CV curves at low scanning speeds of 1, 2, 5 and 10 mV s^{-1} and calculated the proportion of diffusion-controlled process and surface capacitance-control process in the total capacitance using the Dunn formula:[51]

$$i = i_{\text{cap}} = i_{\text{diff}} = k_1\nu + k_2\nu^{1/2} \tag{12}$$

$$i\ (\text{V})/\nu^{1/2} = k_1\nu^{1/2} + k_2 \tag{13}$$

The total current response value at a particular voltage is denoted by i (V), $k_1\nu$ is the current response value of the surface capacitance control process, and $k_2\nu^{1/2}$ is the current response value of diffusion control.

CV curves were obtained at various scan rates (Fig. S9†). The integral area of the closed part of the curve could be used to determine the relative amounts of the two control mechanisms. It was found that the surface capacitance control of NCO/MNC-LDH accounts for 83.1%, 84.6%, 87.8% and 93.9% of the total capacitance at scan rates 1, 2, 5 and 10 mV s^{-1}, respectively (Fig. 7b). The contribution of the surface capacitance-controlled process was shown to rise with the scan rate. This was connected to the quickly reversible redox reaction with electrolyte ions that occurs on or near the electrode surface.[52] Meanwhile, regardless of the scan rate, the surface capacitance-controlled process contribution of NCO/MNC-LDH was larger than the other four samples, which further confirmed that crystalline/amorphous composite structures were more favorable for reaction kinetics (Table 1). This phenomenon can be explained by the construction of the hierarchical and three-dimensional pompom-like structure composed of ultrathin nanoflakes, which leads to NCO/MNC-LDH with a small volume and increased exposure area. The redox reaction was no longer restricted to the bulk due to the increased specific surface area, but essentially transformed into a surface redox reaction, with a significantly shortened ion diffusion length and reduced diffusion limitation. At the same time, the amorphous material provided more ion transfer channels, which was mainly manifested in the surface capacitive control process.

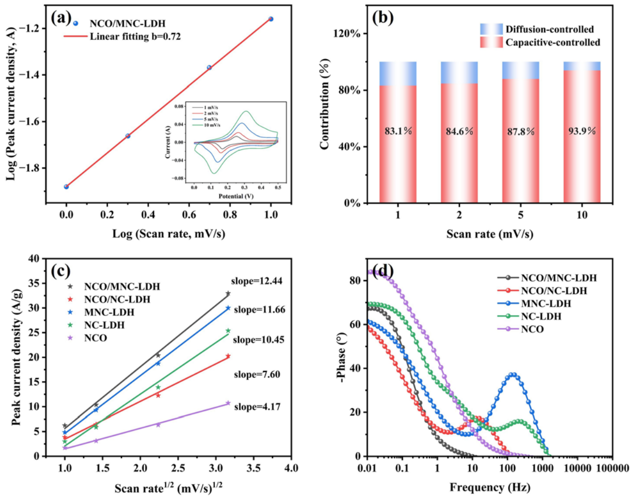

Fig. 7 (a) Log i–log v plot of NCO/MNC-LDH; (b) comparison of charge storage for NCO/MNC-LDH by diffusion and capacitive control; (c) the relationship between anodic peak current densities and the square root of scan rates for NCO/MNC-LDH, NCO/NC-LDH, MNC-LDH, NC-LDH and NCO electrodes; and (d) Bode plots of NCO/MNC-LDH, NCO/NC-LDH, MNC-LDH, NC-LDH and NCO.

Table 1 The contribution ratio of the surface capacitive-controlled process of NCO, NC-LDH, MNC-LDH, NCO/NC-LDH, and NCO/MNC-LDH samples

Sample	1 mV s^{-1}	2 mV s^{-1}	5 mV s^{-1}	10 mV s^{-1}
NCO	64.0%	68.2%	75.9%	85.1%
NC-LDH	64.5%	73.9%	80.8%	87.24%
MNC-LDH	40.5%	46.2%	56.3%	68.2%
NCO/NC-LDH	29.3%	34.4%	46.4%	56.0%
NCO/MNC-LDH	83.1%	84.6%	87.8%	93.9%

The anodic peak current density (I_p) of the NCO/MNC-LDH electrode materials was linearly correlated with the square root of scan rate ($\nu^{1/2}$), demonstrating that its redox reactions were dominated by diffusion control (battery-type behavior) (Fig. 7c).[53–55] The diffusion coefficient (D) of OH^- of various materials may be computed and examined through the Randles–Sevcik equation.[56]

$$I_p = (2.687 \times 10^5)n^{3/2}AC\ (\nu D)^{1/2} \tag{14}$$

where A, n, and C refer to the surface area of the electrode, the number of electrons participating in the redox reaction, and the proton concentration, respectively.

Therefore,

$$\frac{D_{\text{NCO/MNC-LDH}}}{D_{\text{NCO}}} = \left(\frac{(I_p/\nu^{1/2})_{(\text{NCO/MNC-LDH})}}{(I_p/\nu^{1/2})_{(\text{NCO})}}\right)^2 = \left(\frac{12.44}{4.17}\right)^2 = 8.90 \tag{15}$$

The calculated result showed that the OH^- diffusion coefficient of the NCO/MNC-LDH electrode material was 8.9 times that of NCO. Through the comparison of the five materials, it was found that NCO/MNC-LDH exhibited a faster OH^- diffusion rate.[57] This was due to the nanosheet array structure and larger SSA of the prepared material, which allowed electrolyte ions to diffuse into the electrode more quickly. More importantly, amorphous materials can enrich ion transfer channels.[2]

The Bode diagrams for the five materials are displayed in Fig. 7d. NCO/MNC-LDH, NCO/NC-LDH, MNC-LDH, NC-LDH, and NCO exhibited phase angles of −67.2°, −58.7°, −61.5°, −69.3°, and −83.8°, in that order. The closer ideal capacitance behavior (−90°) of the crystalline/amorphous composite could be demonstrated by the higher phase angle of NCO/MNC-LDH compared to those of NCO/NC-LDH and MNC-LDH.[58]

The electrochemical surface area (ECSA) is intrinsically linked to the density of active sites, thus serving as a critical parameter governing overall electrochemical performance. Fig. S10† shows the CV curves of each material in the non-faradaic region at varying scan rates (10, 20, 40, 60 and 80 mV s^{-1}), accompanied by the calculated double-layer capacitance (C_{dl}) and derived electrochemically active surface area (ECSA) values (Fig. S11†). It is impressive that NCO/MNC-LDH exhibited the largest C_{dl} of 0.75 mF cm^{-2} along with the highest ECSA of 18.75 cm^2, surpassing other materials. This demonstrates that the constructed crystalline/amorphous phase composite material can provide more active sites for redox reactions.

3.4. Electrochemical performance of the NCO/MNC-LDH//AC HSC device

In order to test the actual application performance of the prepared sample, it was necessary to assemble NCO/MNC-LDH into HSC devices. First, the electrochemical performance of AC needs to be evaluated for the purpose of matching the positive and negative electrodes (Fig. S12†). The mass matching formula mentioned above was used to determine the theoretical mass loading of the two electrodes. Fig. 8a shows the assembly diagram of a HSC device. The CV curves of the positive and negative electrodes at 10 mV s^{-1} are displayed in Fig. 8b, illustrating that the constructed HSC device can work in the voltage range of 0–1.7 V. Additionally, further study was carried out on the NCO/MNC-LDH//AC CV curves in various voltage windows (Fig. 8c). The NCO/MNC-LDH//AC device exhibited a consistent CV curve shape and no polarization phenomenon when it ran in the voltage window of 1.6–1.7 V. The polarization phenomena of the CV curve appeared as the voltage window widened to 1.8 V, suggesting that this HSC device can operate normally in multiple voltage windows (1.6 and 1.7 V). Fig. 8d shows the CV images of HSC devices at various scan rates (10–50 mV s^{-1}). The overall shape of the CV curve essentially stayed the same as the scan rate rose gradually. The HSC devices exhibited fast ion diffusion, fast redox reactions, and good rate characteristics. Likewise, the asymmetrical shape of the GCD graphs confirmed this feature (Fig. 8e). Fig. S13† shows the CV and GCD graphs of HSC devices composed of four other materials and AC, respectively. At 1, 2, 3, 5, and 10 A g^{-1}, the specific capacitance of the NCO/MDC-LDH//AC HSC device was 143.5, 132.1, 124.1, 112.9, and 92.4 F g^{-1}, in that order (Fig. 8f), which were higher than those of NCO//AC, NC-LDH//AC, MNC/LDH//AC, and NCO/NC LDH//AC HSC devices, respectively. After 20 000 successive charge and discharge cycles, the NCO/MNC-LDH//AC HSC device demonstrated good electrochemical reversibility and cycling stability at 5 A g^{-1}, maintaining 76.3% of the initial specific capacitance and maintaining a 100% coulombic efficiency (Fig. 8g).

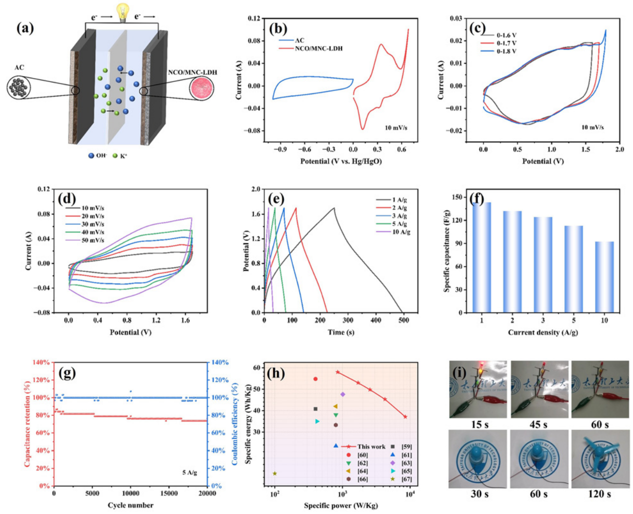

Fig. 8 (a) HSC device diagram; (b) CV curves of AC and NCO/MNC-LDH at 10 mV s^{-1}; (c) CV curves in different voltage windows; (d) CV curves at 10–50 mV s^{-1} in 0–1.7 V; (e) GCD curves at 1–10 A g^{-1}; (f) specific capacitances at different current densities; (g) cycling stability and Coulomb efficiency; (h) Ragone plots; and (i) the LEDs and mini electric fan driven by the NCO/MNC-LDH//AC device.

CV and GCD curves before and after the cycles are shown in Fig. S14.† Fig. 8h displays the Ragone plots of NCO/MNC-LDH//AC and other relevant HSC devices. The energy density could reach 58 Wh kg^{-1} at a power density of 850 W kg^{-1} and it remained at 37.1 Wh kg^{-1} at a power density of 8500 W kg^{-1}, which was better than those of several comparable HSC devices that have been previously reported, such as NiCoP@NiCo-B-70//AC (40.8 Wh kg^{-1} at 400 W kg^{-1}),[59] crystalline/amorphous Co_3S_4//AC (54.78 Wh kg^{-1} at 400.02 W kg^{-1}),[60] NCM-S@HCNS//3D N-rGO (23.5 Wh kg^{-1} at 800.4 W kg^{-1}),[61] Mo-NiS_2@NiCo-LDH//AC (38.1 Wh kg^{-1} at 800 W kg^{-1}),[62] Co–Mo–S//AC (47.6 Wh kg^{-1} at 1012.9 W kg^{-1}),[63] NiCo-LDH@CoP@NiCo-P//AC (42 Wh kg^{-1} at 800 W kg^{-1}),[64] 0.5Mo-NiCo_2O_4//AC (35 Wh kg^{-1} at 420 W kg^{-1}),[65] Mn$Co_2O_{4.5}$@NiCo-LDH//AC (33.3 Wh kg^{-1} at 798 W kg^{-1}),[66] and NiMn-LDH@CuO//AC (10.8 Wh kg^{-1} at 100 W kg^{-1}).[67] Table S4† shows the comparison between our work and other previous works. The research results demonstrated that the prepared NCO/MNC-LDH composite material exhibited excellent electrochemical performance, showing promising application prospects.

4. Conclusions

To summarize, a novel crystalline NCO/amorphous MNC-LDH electrode material was successfully prepared in this work. Due to the achievement of a balance between electrochemical activity and stability by the crystalline/amorphous composite, it demonstrated excellent electrochemical characteristics. The specific capacity of 841 C g^{-1} at 1 A g^{-1} and 82.3% of the specific capacity at 20 A g^{-1} indicated that NCO/MNC-LDH exhibited a good energy storage capacity. The assembled NCO/MNC-LDH//AC HSC device displayed a high energy density of 58 Wh kg^{-1} at a power density of 850 W kg^{-1} and still maintained an energy density of 37.1 Wh kg^{-1} when the power density increased to 8500 W kg^{-1}. This work provides a simple and feasible method for preparing crystalline/amorphous composite materials and facilitates the development of supercapacitors.

Author contributions

Juan Lei: conceptualization, data curation, funding acquisition, supervision, writing – original draft, and writing – review & editing. Yan Zhang: conceptualization, data curation, formal analysis, and writing – original draft. YuJing Wang: formal analysis, writing – original draft, and writing – review & editing. Xiaoli Ren: conceptualization, investigation, and formal analysis. Lijun Cheng: methodology and data curation. Qinqin He: supervision. Shuang Wang: funding acquisition, supervision, writing – original draft, and writing – review & editing.

Conflicts of interest

The authors declare no conflict of interest.

Data availability

The data supporting this article have been included as part of the ESI.†

Acknowledgements

The authors acknowledge the financial support from the National Natural Science Foundation of China (Grant No. 22408252), the Natural Science Foundation of Shanxi Province (Grant No. 202403021221035) and the Taiyuan Institute of Technology Talent Introduction Research Funding Project (2022KJ010).

References

1 X. Tang, J. Wang, D. Zhang, B. Wang, X. Xia, X. Meng, B. Yang, J. Chen, Y. He and Z. Han, *Chem. Eng. J.*, 2023, **452**, 139429.

2 B. Huang, J. Yuan, Y. Lu, Y. Zhao, X. Qian, H. Xu, G. He and H. Chen, *Chem. Eng. J.*, 2022, **436**, 135231.

3 P. F. Yin, M. Zhou, J. Chen, C. Tan, G. Liu, Q. Ma, Q. Yun, X. Zhang, H. Cheng, Q. Lu, B. Chen, Y. Chen, Z. Zhang, J. Huang, D. Hu, J. Wang, Q. Liu, Z. Luo, Z. Liu, Y. Ge, X. J. Wu, X. W. Du and H. Zhang, *Adv. Mater.*, 2020, **32**, 2000482.

4 D. Merki, S. Fierro, H. Vrubel and X. Hu, *Chem. Sci.*, 2011, **2**, 1262–1267.

5 N. Yang, H. Cheng, X. Liu, Q. Yun, Y. Chen, B. Li, B. Chen, Z. Zhang, X. Chen, Q. Lu, J. Huang, Y. Huang, Y. Zong, Y. Yang, L. Gu and H. Zhang, *Adv. Mater.*, 2018, **30**, 1803234.

6 G. Chen, Y. Zhu, H. M. Chen, Z. Hu, S. F. Hung, N. Ma, J. Dai, H. J. Lin, C. T. Chen, W. Zhou and Z. Shao, *Adv. Mater.*, 2019, **31**, 1900883.

7 H. Han, H. Choi, S. Mhin, Y.-R. Hong, K. M. Kim, J. Kwon, G. Ali, K. Y. Chung, M. Je, H. N. Umh, D.-H. Lim, K. Davey, S.-Z. Qiao, U. Paik and T. Song, *Energy Environ. Sci.*, 2019, **12**, 2443–2454.

8 J. S. Kim, I. Park, E. S. Jeong, K. Jin, W. M. Seong, G. Yoon, H. Kim, B. Kim, K. T. Nam and K. Kang, *Adv. Mater.*, 2017, **29**, 1606893.

9 J. M. V. Nsanzimana, Y. Peng, Y. Y. Xu, L. Thia, C. Wang, B. Y. Xia and X. Wang, *Adv. Energy Mater.*, 2017, **8**, 1701475.

10 Y. Wang, X. Li, Z. Huang, H. Wang, Z. Chen, J. Zhang, X. Zheng, Y. Deng and W. Hu, *Angew. Chem., Int. Ed.*, 2023, **62**, e202215256.

11 W. L. Xue, W. H. Deng, H. Chen, R. H. Liu, J. M. Taylor, Y. k. Li, L. Wang, Y. H. Deng, W. H. Li, Y. Y. Wen, G. E. Wang, C. Q. Wan and G. Xu, *Angew. Chem., Int. Ed.*, 2020, **60**, 1290–1297.

12 D. Zhou, X. Su, M. Boese, R. Wang and H. Zhang, *Nano Energy*, 2014, **5**, 52–59.

13 D. Gao, Y. Pan, J. Wei, D. Han, P. Xu, Y. Wei, L. Mao and X. Yin, *J. Mater. Chem.*, 2022, **10**, 11186–11195.

14 D. Wang, J. Wang, Y. Chu, S. Zha, Y. Chen, X. Du, N. Mitsuzaki, S. Jia and Z. Chen, *J. Energy Storage*, 2024, **96**, 112614.

15 X. Huang, Y. Huang, G. Xu and X. Wang, *J. Power Sources*, 2023, **581**, 233488.

16 J. Zhang, Y. Li, Z. Chen, Q. Liu, Q. Chen and M. Chen, *Energy Environ. Mater.*, 2023, **6**, 1801495.

17 X. Wang, Y. Tuo, Y. Zhou, D. Wang, S. Wang and J. Zhang, *Chem. Eng. J.*, 2021, **403**, 126297.

18 M. Yu, J. Zheng and M. Guo, *J. Energy Chem.*, 2022, **70**, 472–479.

19 Q. Ding, J. Yin, J. Li, S. Li, C. Chen, S. Sun, Y. Xu and H. Li, *Mater. Today Chem.*, 2024, **36**, 101935.

20 C. Guan, W. Xiao, H. Wu, X. Liu, W. Zang, H. Zhang, J. Ding, Y. P. Feng, S. J. Pennycook and J. Wang, *Nano Energy*, 2018, **48**, 73–80.

21 Y. T. Xu, Z. M. Ye, J. W. Ye, L. M. Cao, R. K. Huang, J. X. Wu, D. D. Zhou, X. F. Zhang, C. T. He, J. P. Zhang and X. M. Chen, *Angew. Chem., Int. Ed.*, 2018, **58**, 139–143.

22 A. Ali, M. Aadil, A. Rasheed, I. Hameed, S. Ajmal, I. Shakir and M. F. Warsi, *Synth. Met.*, 2020, **265**, 116408.

23 W. Liu, L. Yu, R. Yin, X. Xu, J. Feng, X. Jiang, D. Zheng, X. Gao, X. Gao, W. Que, P. Ruan, F. Wu, W. Shi and X. Cao, *Small*, 2020, **16**, 1906775.

24 J. Lin, H. Jia, H. Liang, S. Chen, Y. Cai, J. Qi, C. Qu, J. Cao, W. Fei and J. Feng, *Adv. Sci.*, 2017, **5**, 1700687.

25 J. Fu, L. Li, J. M. Yun, D. Lee, B. K. Ryu and K. H. Kim, *Chem. Eng. J.*, 2019, **375**, 121939.

26 Y. Shao, M. F. El-Kady, J. Sun, Y. Li, Q. Zhang, M. Zhu, H. Wang, B. Dunn and R. B. Kaner, *Chem. Rev.*, 2018, **118**, 9233–9280.

27 D. Zha, Y. Fu, L. Zhang, J. Zhu and X. Wang, *J. Power Sources*, 2018, **378**, 31–39.

28 K. P. Annamalai, L. Liu and Y. Tao, *J. Mater. Chem. A*, 2017, **5**, 9991–9997.

29 X.-h. Xia, J.-p. Tu, Y.-q. Zhang, Y.-j. Mai, X.-l. Wang, C.-d. Gu and X.-b. Zhao, *RSC Adv.*, 2012, **2**, 1835–1841.

30 G. Gao, H. B. Wu, S. Ding, L.-M. Liu and X. W. D. Lou, *Small*, 2015, **11**, 804–808.

31 W. Hu, L. Chen, B. Geng, M. Du, G. Shan, Y. Song, Z. Wu and Q. Zheng, *ACS Appl. Energy Mater.*, 2023, **6**, 2781–2792.

32 C. Huang, Y. Hu, S. Jiang and H. C. Chen, *Electrochim. Acta*, 2019, **325**, 134936.

33 C. Huang, X. Song, Y. Qin, B. Xu and H. C. Chen, *J. Mater. Chem.*, 2018, **6**, 21047–21055.

34 H. Chen, L. Hu, M. Chen, Y. Yan and L. Wu, *Adv. Funct. Mater.*, 2013, **24**, 934–942.

35 D. Xia, H. Chen, J. Jiang, L. Zhang, Y. Zhao, D. Guo and J. Yu, *Electrochim. Acta*, 2015, **156**, 108–114.

36 M. Li, K. Y. Ma, J. P. Cheng, D. Lv and X. B. Zhang, *J. Power Sources*, 2015, **286**, 438–444.

37 G. Wang, K. Qi, Z. Yan, L. Yue, Y. Ding, W. Li and Z. Xu, *Appl. Surf. Sci.*, 2022, **592**, 153293.

38 B. Dahal, T. Mukhiya, G. P. Ojha, K. Chhetri, A. P. Tiwari, A. Muthurasu, M. Lee, S.-H. Chae, T. Kim, D. C. Chung and H. Y. Kim, *Chem. Eng. J.*, 2020, **387**, 124028.

39 W. Hu, L. Chen, B. Geng, Y. Song, Z. Wu, Q. Zheng, G. Shan and M. Du, *Chem. Eng. J.*, 2023, **468**, 143694.

40 X. Xu and J. I. Han, *Surf. Interfaces*, 2022, **30**, 101896.

41 X. Shan, Z. Guo, Z. Qu, Y. Zou, L. Zhao and P. Chen, *Mater. Res. Lett.*, 2022, **10**, 593–601.

42 Y. Ding, Z. Yan, G. Wang, H. Sang, Z. Xu and W. Li, *Small*, 2023, **20**, 2302388.

43 D. D. Khumujam, T. Kshetri, T. I. Singh, N. H. Kim and J. H. Lee, *Adv. Funct. Mater.*, 2023, **33**, 2302388.

44 J. Balamurugan, T. T. Nguyen, V. Aravindan, N. H. Kim, S. H. Lee and J. H. Lee, *Nano Energy*, 2019, **65**, 103999.

45 Y. Jiang and J. Liu, *Energy Environ. Mater.*, 2019, **2**, 30–37.

46 L. Huang, H. Huang, W. Guo and S. Wang, *Electrochim. Acta*, 2022, **434**, 141317.

47 S. Li, Y. Luo, C. Wang, M. Wu, Y. Xue, J. Yang and L. Li, *J. Alloys Compd.*, 2022, **920**, 165986.

48 W. Hu, B. Hu, Z. Wu, M. Zuo, Y. Song, Q. Zheng, G. Shan and M. Du, *Small Struct.*, 2024, **5**, 2300574.

49 L. Zhang, P. Cai, Z. Wei, T. Liu, J. Yu, A. A. Al-Ghamdi and S. Wageh, *J. Colloid Interface Sci.*, 2021, **588**, 637–645.

50 I. Hussain, T. Hussain, S. Yang, Y. Chen, J. Zhou, X. Ma, N. Abbas, C. Lamiel and K. Zhang, *Chem. Eng. J.*, 2021, **413**, 127570.

51 T.-C. Liu, W. G. Pel and B. E. Conway, *J. Electrochem. Soc.*, 1998, **145**, 1882.

52 M. Wang, S. Wang, J. Zhao, S. Li, J. Wang, J. Mi and Y. Feng, *Chem. Eng. J.*, 2024, **480**, 148206.

53 Y. Fu, Y. Zhou, Q. Peng, C. Yu, Z. Wu, J. Sun, J. Zhu and X. Wang, *J. Power Sources*, 2018, **402**, 43–52.

54 J. Liu, J. Wang, Z. Ku, H. Wang, S. Chen, L. Zhang, J. Lin and Z. X. Shen, *ACS Nano*, 2015, **10**, 1007–1016.

55 T. Nguyen and M. F. Montemor, *J. Mater. Chem. A*, 2018, **6**, 2612–2624.

56 L. Li, K. S. Hui, K. N. Hui, T. Zhang, J. Fu and Y.-R. Cho, *Chem. Eng. J.*, 2018, **348**, 338–349.

57 D. Zha, H. Sun, Y. Fu, X. Ouyang and X. Wang, *Electrochim. Acta*, 2017, **236**, 18–27.

58 B. Sun, X. Fan, R. Hou, G. Zhao, Q. Liu, H. Zhou and P. Liang, *Chem. Eng. J.*, 2023, **454**, 140280.

59 M. Shi, M. Zhao, Q. Zheng, F. Li, L. Jiao, Z. Su, M. Li and X. Song, *Energy Fuels*, 2024, **38**, 1525–1537.

60 M. Liang, M. Zhao, H. Wang, Q. Zheng and X. Song, *J. Mater. Chem.*, 2018, **6**, 21350–21359.

61 Y. Zhou, Z. Jia, S. Zhao, P. Chen, Y. Wang, T. Guo, L. Wei, X. Cui, X. Ouyang, X. Wang, J. Zhu, J. Sun, S. Pan and Y. Fu, *Chem. Eng. J.*, 2021, **416**, 129500.

62 M. Shi, M. Zhao, L. Jiao, Z. Su, M. Li and X. Song, *J. Power Sources*, 2021, **509**, 230333.

63 Z.-X. Wu, L.-Q. Fan, J.-J. Chen, X.-G. Deng, T. Tang, Y.-F. Huang and J.-H. Wu, *J. Colloid Interface Sci.*, 2023, **649**, 880–889.

64 P. Li, X. Wang, S. Yang, K. Chu, H. Zhang, D. Chen and Q. Li, *Mater. Today Chem.*, 2024, **41**, 102274.

65 S. Xiong, L. Wang, H. Chai, Y. Xu, Y. Jiao and J. Chen, *J. Colloid Interface Sci.*, 2022, **606**, 1695–1706.

66 H. Zhang, T. Xiong, R. Chen, Y. Wang, C. Fang, L. Xu and C. Liu, *Electrochim. Acta*, 2023, **455**, 142412.

67 A. Zhang, W. Zheng, Z. Yuan, J. Tian, L. Yue, R. Zheng, D. Wei and J. Liu, *Chem. Eng. J.*, 2020, **380**, 122486.